

Satellite Parallaxes of Lensing Events Towards the Galactic Bulge

B. Scott Gaudi

and

Andrew Gould*

Dept. of Astronomy, The Ohio State University, Columbus, OH 43210

e-mail gaudi@payne.mps.ohio-state.edu

e-mail gould@payne.mps.ohio-state.edu

Abstract

In order to understand the nature of the lenses that generate microlensing events, one would like to measure their mass, distance, and velocity. Unfortunately, current microlensing experiments measure only one parameter of the events, the characteristic timescale, which is a combination of the underlying physical parameters. Other methods are required to extract additional information. Parallax measurements using a satellite in an Earth-like orbit yield the projected velocity of the lens: $\tilde{\mathbf{v}} = \mathbf{v}/(1-z)$, where \mathbf{v} is the transverse velocity (speed and direction) of the lens relative to the Earth-source line of sight, and z is the ratio of the distances to the lens and the source. A measurement of $\tilde{\mathbf{v}}$ could distinguish between lenses belonging to the bulge and disk populations. We show that for photometric precisions of 1% to 2%, it is possible to measure the projected speed, \tilde{v} , to an accuracy of $\leq 10\%$ for over 70% of disk lenses and over 60% of bulge lenses. For measuring the projected velocity $\tilde{\mathbf{v}}$, the percentages are 40% and 30%, respectively. We find lines of sight $> 2^\circ$ away from the ecliptic are preferable, and an Earth-satellite separation in the range 0.7AU – 1.9AU is optimal. The requirements of the satellite for measuring the projected velocities of events towards the bulge are similar to those for measurements toward the LMC.

Subject Headings: gravitational lensing – Galaxy: stellar content
submitted to *The Astrophysical Journal*: January 9, 1995
Preprint: OSU-TA-1/96

* Alfred P. Sloan Foundation Fellow

1. Introduction

Four ongoing microlensing searches have detected more than 100 candidate events, the great majority toward the Galactic bulge. The MACHO collaboration (Alcock et al. 1995b, 1996b) have reported 8 candidate microlensing events of stars in the Large Magellanic Cloud (LMC), more than expected by the known luminous stars of the Milky Way (Bahcall et al. 1994; Gould, Bahcall & Flynn 1996) and LMC (Gould 1995b), but less than expected from standard spherical halo models (Paczynski 1986; Griest 1991). The EROS collaboration (Aubourg et al. 1995, Ansari et al. 1996) have reported 2 candidate events towards the LMC. The MACHO (Alcock et al. 1995a, 1996a), OGLE (Udalski et al. 1994), and DUO (Alard 1996) collaborations have reported more than 100 candidate events of stars towards the galactic bulge. This is also more than expected by known stars. These discrepancies suggest that a revision of the current models of the structure of the disk, bulge, and halo may be in order.

The light curve generated by a microlensing event is described by the magnification $A(x) = (x^2 + 2)/x(x^2 + 4)^{1/2}$, where $x(t)$ is the position of the lens in the Einstein ring as a function of time, and is given by, $x(t) = [\omega^2(t - t_0)^2 + \beta^2]^{1/2}$. Here t_0 is the time of maximum magnification, β is the impact parameter in units of the Einstein ring radius, and $\omega = t_e^{-1}$ is the inverse Einstein ring crossing time. Thus the magnification curve is fit by three parameters, ω, β, t_0 . Of these three parameters, only ω yields any information about the lens itself; β and t_0 reflect only the geometry of the event. The timescale is related to the Einstein ring radius and velocity of the lens by $t_e = r_e/v$. Here $v = |\mathbf{v}|$ is the magnitude of the transverse velocity of the lens along the Earth-source line of sight,

$$\mathbf{v} = \mathbf{v}_l - \left[\mathbf{v}_s \frac{d_{ol}}{d_{os}} + \mathbf{v}_o \frac{d_{ls}}{d_{os}} \right], \quad (1.1)$$

where \mathbf{v}_s , \mathbf{v}_l , and \mathbf{v}_o are the transverse velocities of the source, lens and observer, respectively, d_{ol} and d_{os} are the distances to the lens and source, and d_{ls} is the

distance between the lens and the source. The Einstein ring radius is defined,

$$r_e^2 = \frac{4GM}{c^2} d_{\text{os}} z (1 - z), \quad z = \frac{d_{\text{ol}}}{d_{\text{os}}}. \quad (1.2)$$

Thus the timescale is a combination of the lens's physical characteristics: M , d_{ol} , and v . Because the bulge and disk of the Galaxy are characterized by different speed and distance distributions, separate measurements of v and d_{ol} would allow one to determine the component to which the lens belongs. Measurement of M would yield the mass spectrum of lenses in these components. Unfortunately, a measurement of t_e alone provides no direct information about these characteristics. Some information can be obtained by considering probability distributions, but this method is inherently statistical in nature. Furthermore, lenses belonging to the Galactic bulge will produce events with time scales very similar to those produced by lenses belonging to the Galactic disk. As a result, measurements of t_e alone differentiate poorly between these two components.

In order to discriminate between the bulge and disk components, one must consider methods of extracting more information from each event. Several methods have been proposed, including using parallax to measure the projected velocity of the lens, $\tilde{\mathbf{v}} \equiv \mathbf{v}/(1 - z)$. There are two basic methods of acquiring information from parallax: ground-based measurements and space-based measurements. The projected velocity of one lens has already been measured using ground-based parallax (Alcock et al. 1995c). However, ground-based parallax is limited to those events for which the crossing time is large, $t_e \gtrsim 2$ months; it is only for these events that the motion of the Earth induces measurable asymmetries in the light curve. Unfortunately, most of the events that have been detected so far have time scales significantly smaller than those required for ground-based parallax.

Ground-based parallax illustrates a generic problem inherent in most of the methods that have been proposed for measuring the physical characteristics of lenses. These methods are only effective for a small fraction of events. Furthermore, those events for which these methods are viable typically represent a very biased subsample. Measurements of proper motions are biased towards bulge events,

color-shift measurements are biased towards bright lenses, and ground-based parallax measurements are biased toward events with long durations. In contrast, satellite-based parallax measurements are effective for a majority of events, and are not biased towards a particular class of events.

Two basic methods have been suggested of measuring the proper motion of the lens, $\mu = v/d_{\text{ol}}$. These are photometric (Gould 1994; Nemiroff & Wickramasinghe 1994; Witt & Mao 1995; Witt 1995; Loeb & Sasselov 1995; Gould & Welch 1996) and spectroscopic (Maoz & Gould 1994). Ideally one would like to combine measurements of both the proper motion and the parallax to determine both \tilde{v} and μ . These two parameters, along with the timescale, completely determine M , d_{ol} , and v (Gould 1996). (Combined measurements of the proper motion and parallax can be used to determine the true velocity of the lens only if the projected velocity, $\tilde{\mathbf{v}}$, is determined, and not just the projected speed \tilde{v} .) As we discuss below, parallax measurements can be used to determine $\tilde{\mathbf{v}}$ in a significant fraction of events. Thus the mass spectrum, physical distribution, and velocity distribution of lenses could be determined if both the parallax and proper motion of events could be measured. Unfortunately, while optical interferometers may be able to measure proper motions for many events in the relatively near future, events for which proper motion can currently be measured are rare.

It is not strictly necessary, however, to measure both μ and \tilde{v} in order to distinguish between component populations of lenses. Han & Gould (1995) demonstrated that, for events towards the galactic bulge, the typical values of \tilde{v} are reasonably well separated. Thus a measurement of \tilde{v} alone, gathered from parallax information, can be used to determine the component to which the lens belongs. Furthermore, parallax measurements can often be used to determine not only \tilde{v} , but also the projected velocity of the lens, $\tilde{\mathbf{v}}$. Information about $\tilde{\mathbf{v}}$ is even more useful in distinguishing between bulge and disk populations (Han & Gould 1995).

Space-based parallax is the most promising method of extracting information about lenses. Gould (1995a) demonstrated the basic method of using information

obtained by a satellite in an Earth-like orbit to measure $\tilde{\mathbf{v}}$, and also gave a rough estimate of the photometric precision needed. Due to parallax, the light curve of a particular microlensing event will be different as seen from the Earth and the satellite. This difference is given by the vector displacement of the lens in the Einstein ring, $\Delta\mathbf{x} \equiv (\omega\Delta t, \Delta\beta)$. Here Δt is the difference between the time of maximum magnification for the Earth and satellite, $\Delta t = t'_0 - t_0$, and $\Delta\beta$ is the difference between the impact parameters, $\Delta\beta = \beta' - \beta$. The vector displacement is related to the Earth-satellite separation by

$$\Delta\mathbf{x} = \frac{\mathbf{r}}{\tilde{r}_e}, \quad (1.3)$$

where \mathbf{r} is the projection of the Earth-satellite separation vector \mathbf{R} , onto the plane of the sky (perpendicular to the source vector $\hat{\mathbf{s}}$), and \tilde{r}_e is the projected Einstein ring radius,

$$\tilde{r}_e = \frac{r_e}{1 - z}. \quad (1.4)$$

Thus by measuring t_0 and β for the Earth and the satellite, one can determine the projected Einstein ring radius, and this, combined with the timescale t_e , can be used to calculate the projected velocity of the lens, $\tilde{\mathbf{v}}$.

Complications arise from the fact that there is a four-fold degeneracy inherent in the determination of $\tilde{\mathbf{v}}$, including a two-fold degeneracy in the projected speed, \tilde{v} . These degenerate cases arise from the fact the one does not know *a priori* which side of the lens-source line the Earth and the satellite are on. Thus $\Delta\beta$ can have two magnitudes: $\Delta\beta_{\pm} = |\beta' \pm \beta|$, and two distinct signs: $\pm\Delta\beta_{\pm} = \pm|\beta' \pm \beta|$, for a total of four degenerate cases. This degeneracy can, in principle, be broken by measuring the small difference in inverse time scales, $\Delta\omega = \omega' - \omega$, caused by the relative velocity of the Earth and the satellite (Gould 1995a).

Launching a satellite for observing microlensing would be a major undertaking. It is often suggested that the most economical approach would be to attach the telescope to an already planned mission. It turns out, however, that the stability

requirements for observations of microlensing events are such that it would be more economical to launch a dedicated satellite. The primary concern, therefore, is that such a dedicated satellite would be sufficiently versatile and beneficial to justify the expense. We have already discussed what could be gained from a measurement of $\tilde{\mathbf{v}}$ of lenses, but it remains to be shown that a satellite with reasonable specifications will actually enable one to measure $\tilde{\mathbf{v}}$, and whether these measurements could be made for a large class of microlensing events. There is the further consideration that there are two distinct lines of sight of microlensing observations, the LMC and the galactic bulge. The times of year when these two lines of sight can be observed from the ground are complementary, and one would like one satellite to be able to make measurements for both cases. Since the two cases are markedly different in the nature of events that are expected, the brightness of the source stars being observed, and in the geometry of the parallax measurements, it is not obvious that a satellite with specifications suited to LMC parallax measurements will also be able to make parallax measurements towards the galactic bulge.

It is interesting to ask what the required lifetime of a parallax satellite would be to achieve a reasonable statistical sample of microlensing events. Gould (1995a) estimated that ~ 100 giant star events will be seen towards the bulge during each ~ 6 month bulge season. To observe each event 80 times requires observing ~ 44 events per day, or one event every ~ 30 minutes. The source stars will be typically $I \lesssim 17$, thus to achieve 2% photometry requires observations of ~ 10 minutes on a 25 cm telescope. It is therefore possible to make measurements with 2% photometry for all ~ 100 events. As we discuss below, it is possible to measure the projected speed for $\sim 70\%$ of these events. Gould (1996) estimates that $\sim 15\%$ of giant events could yield measurements of the proper motion, μ . Thus for a satellite lifetime of 3 years, we could expect to use combined parallax and proper motion information to measure the mass and distance of ~ 45 lenses.

In our analysis, we choose to assume that the satellite is on an Earth-like orbit, separated from the Earth by a distance d_{sat} . As we show in the Appendix, this orbit well approximates a realistic orbit in which the satellite has a small velocity

relative to the Earth at the time of launch. Such an orbit is attractive on practical grounds since it requires the least amount of energy to attain. Other orbits, such as those inclined to the ecliptic plane, or with highly eccentric orbits, require a much larger velocity relative to the Earth at the time of launch, and are therefore more expensive to achieve. An Earth-like orbit is therefore optimal for the analysis because it is simplest to study and is the most feasible. As we demonstrate below, such an orbit is also advantageous because it allows for parallax measurements towards the LMC and bulge equally well.

In a earlier paper, [Boutreux & Gould \(1996\)](#) used Monte Carlo simulations of observations of microlensing events in the direction of the LMC to determine the conditions needed to measure the projected speed, \tilde{v} and the projected velocity, $\tilde{\mathbf{v}}$. They found that with photometric precisions of 3% for the Earth and 4% for the satellite, and an Earth-satellite separation of $> 0.5\text{AU}$ that it was possible to measure \tilde{v} for 70% and $\tilde{\mathbf{v}}$ for 50% of LMC events. They found that larger d_{sat} were preferable, and that parallax measurements were possible for a broad range of lens masses.

In this paper, we extend the Monte Carlo analysis of [Boutreux & Gould \(1996\)](#) to observations of microlensing events in the direction of the bulge in order to determine if similar satellite requirements are needed for bulge and LMC observations. We have determined the conditions needed to break the degeneracy for a majority of events, and thus to measure the projected speed, \tilde{v} , and the projected velocity, $\tilde{\mathbf{v}}$, to an accuracy of $\leq 10\%$. We consider the effects of the satellite requirements, the photometric precision and Earth-satellite separation, as well as the mass of the lens and the position of the source star, in order to ensure that the parallax measurements will be sensitive to a broad class of events. We also consider the time of year the observations are made, which, as we show, is a critical parameter for bulge observations. As we discuss in § 2.4, it is predominantly for this reason that the analysis of bulge observations is substantially more complicated than that of LMC observations. The reader may wish to review [Boutreux & Gould \(1996\)](#) in order to become familiar with a similar problem in a simpler setting.

2. Measuring $\tilde{\mathbf{v}}$

The ability to measure $\tilde{\mathbf{v}}$ is dependent on a number of different parameters, several of which are tied together in intricate ways. In this section, we define these parameters, and use a qualitative comparison between observations towards LMC and observations towards the bulge to explain how these parameters affect the measurement of the projected velocity. In § 3 we justify these ideas mathematically. We quantify the ability to measure $\tilde{\mathbf{v}}$ by introducing the Degeneracy Breaking Fraction (DBF). The DBF can be thought of as the percentage of events for which the projected velocity can be measured to an accuracy of $\leq 10\%$ for a specified set of the independent parameters.

In order to measure the projected velocity, one must be able to break the degeneracy between the four possible solutions. We formulate a constraint (derived from the difference in inverse timescales), and discard those solutions which do not obey this constraint. We require that those solutions allowed by the constraint have fractional errors which are small, and are close enough that their difference is unimportant. If these requirements are met, we consider the degeneracy broken. We discuss the DBF quantitatively in § 2.3.

2.1. CONSTRAINT CONDITION

We distinguish the four discrete solutions by means of a constraint on the observables, Δt , $\Delta\beta$, and $\Delta\omega$. Here $\Delta\omega \equiv \omega' - \omega$ is the difference in inverse timescales between the satellite and Earth. Those solutions that are unallowed by the constraint at the 3σ level are distinguishable. As we show below, the ability to break the degeneracy is complicated by the fact that the constraint coefficients are strong functions of the time of year.

The constraint is (Gould 1995a)

$$u_{\parallel}\omega\Delta t + u_{\perp}\Delta\beta - r\Delta\omega = 0, \quad (2.1)$$

where \mathbf{u} is the relative Earth-satellite velocity projected onto the plane of the sky,

u_{\perp} and u_{\parallel} are the components of \mathbf{u} perpendicular and parallel to \mathbf{r} , and $r = |\mathbf{r}|$. In order to derive expressions for u_{\perp} , u_{\parallel} , and r , we define α as the angle between the source vector $\hat{\mathbf{s}}$ and the south ecliptic pole, and ψ as the phase of the orbit such that when $\psi = 0$, the projected displacement vector \mathbf{r} is most closely aligned with $\hat{\mathbf{s}}$. We define $\Omega_{\oplus} = 2\pi \text{yr}^{-1}$, and $R = |\mathbf{R}|$ as the magnitude of the Earth-satellite separation vector. The geometry is shown schematically in Figure 1. Using these definitions, we find,

$$\begin{aligned} r &= R[1 - \sin^2 \alpha \cos^2 \psi]^{1/2}, \\ u_{\perp} &= -\Omega_{\oplus} R \frac{R}{r} \cos \alpha, \\ u_{\parallel} &= -\Omega_{\oplus} R \frac{R}{r} \sin^2 \alpha \frac{\sin(2\psi)}{2}. \end{aligned} \tag{2.2}$$

Note that in Gould (1995a) the sign of u_{\parallel} was incorrectly given as positive. We now recast the constraint equation in the form

$$\sum_{i=1}^3 \alpha_i a_i = 0, \tag{2.3}$$

where α_i are the coefficients of the constraint, and a_i are the event observables

$$a_i = (\Delta t, \Delta \beta, \Delta \omega). \tag{2.4}$$

Using this, we find the simplest form for the constraint coefficients is,

$$\alpha_i = [\Omega_{\oplus} \omega \sin^2 \alpha \frac{\sin(2\psi)}{2}, \Omega_{\oplus} \cos \alpha, (1 - \sin^2 \alpha \cos^2 \psi)]. \tag{2.5}$$

In order to break the degeneracy, the constraint equation (2.3) must distinguish between the four degenerate solutions at the 3σ level. But, as we have shown above, the constraint coefficients α_i are dependent on α and ψ , the line of sight of observations and the phase of the orbit. Furthermore, from equations (1.3) and (2.2), we see that the vector displacement $\Delta \mathbf{x}$ is a function of α and ψ . Thus,

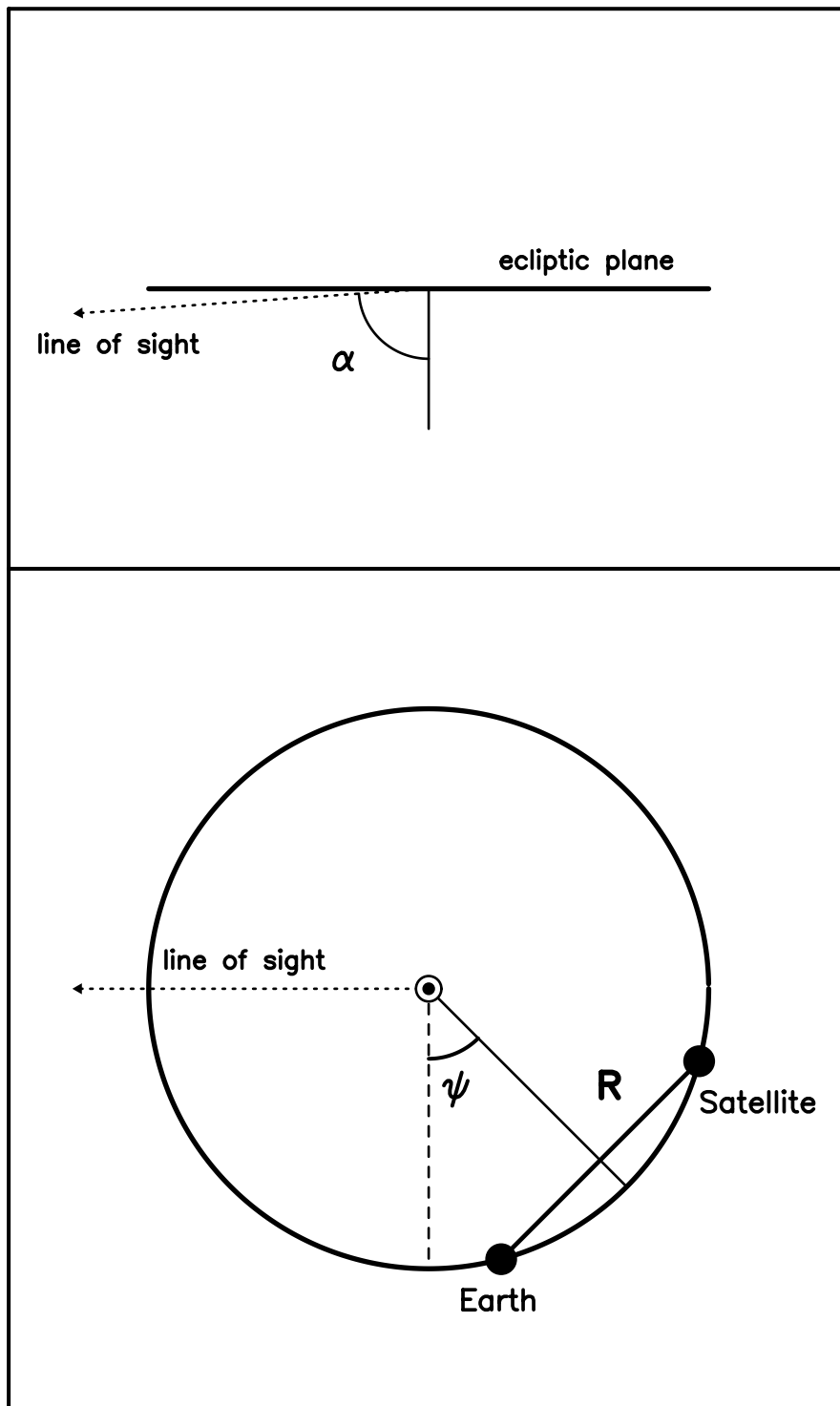


Figure 1. The geometry of the orbits of the Earth and the satellite. Note in particular the angle ψ , defined as the angle such that when $\psi = 0$, the projected displacement vector \mathbf{r} is most closely aligned with the line of sight.

because $\Delta\mathbf{x} \equiv (\omega\Delta t, \Delta\beta)$, the event observables a_i are also functions of α and ψ . All of these contributions are obviously difficult to disentangle, and thus it is not a straightforward matter to describe the conditions under which the constraint equation (2.3) can break the degeneracy.

2.2. FRACTIONAL ERROR

We define the fractional difference as the difference between the allowed solution and the true solution, divided by the true solution. In order that the degeneracy be broken, we require that the fractional errors in the allowed solutions be $< 10\%$. The behavior of the fractional errors is easier to understand than the behavior of the constraint. Roughly speaking, as Δx decreases, the fractional errors rise. Thus, from equation (1.3) we can see that as r decreases, or as \tilde{r}_e increases, the fractional errors rise. From equation (2.2), we see that the projected Earth-satellite separation, r , is a function of direction of the source, α , and the phase of the orbit, ψ . Therefore these parameters affect the fractional error, and thereby affect the DBF.

2.3. DBF AND ERRORS

We define the DBF as the fraction of events for which the degeneracy can be broken for a specified set of parameters. We consider that the degeneracy is broken if the difference between all allowed solutions and the true solution is less than 20% of the true solution, and the fractional error in Δx of each allowed solution is less than 10%. In principle, it could be difficult to characterize the errors in the DBF precisely. This is because there are two distinct types of errors that must be considered. The first is an intrinsic error that arises from the uncertainty in the values of each distinct solution. This error is approximately Gaussian distributed. The second error is characterized by two discrete allowed solutions, and hence is highly non-Gaussian. Taken together, these errors can not be described simply.

We would like to be able to characterize our errors as 10% at the 1σ level. We then consider all possible events with 10% fractional error but with multiple

allowed solutions. If two allowed solutions are separated by 20%, then the 1σ error contour is strongly perturbed by the presence of a second solution, while the 3σ contour is barely affected. On the other hand, if the discrete solutions are 5% apart, then even the 1σ contours are essentially unaffected. Thus, at first sight, the threshold for the allowed separations of distinct solutions appears to depend sensitively on the error contour of interest. In practice, however, the DBF is very nearly the same for 5% and 20% thresholds. See Figure 2, below. In this paper we adopt 20%, which corresponds roughly to focusing on the error contours at the 2σ level.

2.4. LMC VS. BULGE

Observations towards the Galactic bulge are markedly different from those towards the LMC. For observations towards the bulge, the results are complicated by the fact that the ability to break the degeneracy is a strong function of the time of year; this is not the case for observations towards the LMC.

For observations towards the LMC, $\alpha \sim 0$, and from equation (2.2), we find $r = R$, $u_{\parallel} = -R\Omega_{\oplus}$, and $u_{\perp} = 0$. These expressions are obviously independent of ψ . Using equation (2.5), the constraint coefficients become, $\alpha_i = (0, \Omega_{\oplus}, 1)$. Thus the ability to distinguish between the degenerate solutions is independent of the phase of the orbit, and depends only on the photometric precision, the number of observations per crossing time, and the Earth-satellite separation. Given a certain set of parameters, it is therefore possible to quantify the fraction of events for which the degeneracy can be broken, regardless of the phase of the orbit. Furthermore, because r does not vary with ψ , for any given event the fractional errors are also constant throughout the orbit.

The situation is considerably more complicated for bulge observations. For this case, $\alpha \sim 90^\circ$. From equation (2.2), we find that the values of r and u_{\perp} vary as a function of ψ . Therefore the coefficients of the constraint equation (2.5), and hence the ability of the constraint to distinguish between the solutions, are a

strong function of the phase of the orbit. For example, consider Baade's window, for which $\alpha = 84^\circ$. For $\psi = 0$ or 180° , we can approximate the constraint equation as

$$\Delta\beta \simeq -\frac{\Delta\omega}{10\Omega_\oplus}, \quad (2.6)$$

whereas for $\psi = 90^\circ$ or 270° ,

$$\Delta\beta \simeq -\frac{10\Delta\omega}{\Omega_\oplus}. \quad (2.7)$$

We can see from these relations the effect of ψ on the ability of the constraint to distinguish between the degenerate values of $\Delta\beta$. For a specified uncertainty in the value of $\Delta\omega$, the uncertainty in $\Delta\beta$ is 100 times less when $\psi = 0$ or 180° , than when $\psi = 90^\circ$ or 270° . Thus we can expect that, in general, it is easier to distinguish between the degenerate solutions when $\psi = 0$ or 180° than when $\psi = 90^\circ$ or 270° . For intermediate values of ψ , we can interpolate the behavior of the constraint accordingly.

For bulge observations, the intrinsic errors are also strongly dependent on ψ . From equation (2.2) we see that, for observations near $\alpha = 90^\circ$, the projected Earth-satellite separation, r , varies approximately as $\sin\psi$. Thus, from equation (1.3), for $\psi \sim 0$ or 180° , the value of Δx is comparatively small, and therefore the fractional errors are comparatively large, whereas for $\psi \sim 90^\circ$ or 270° , the value of Δx is comparatively large, and thus the fractional errors are comparatively small. As before, we can interpolate the behavior of the fractional errors for intermediate values of ψ .

The effects of ψ on the constraint condition and fractional errors are in competition with each other. We therefore expect the DBF, which is a combination of both of these considerations, to have four minima: when the fractional errors dominate, at $\psi = 0$ or 180° , *and* when the constraint on $\Delta\beta$ is poor, at $\psi \simeq 90^\circ$ or 270° . We expect the maximum values of the DBF to occur where the fractional errors are not dominant, yet the constraint still distinguishes between the degen-

erate solutions reasonably well. In the next section, we review these qualitative arguments in a more precise form.

3. Error Analysis

In this section we give an overview of the mathematical analysis underlying the Monte Carlo code. For a more complete description, we refer the reader to § 2 of *Boutreux & Gould (1996)*; much of the analysis given therein is entirely applicable to the present considerations. The reader who is primarily interested in the results can skip this section entirely.

The flux $F(t)$ from a microlensed star is a function of five parameters, $a_i = (t_0, \beta, \omega, F_0, B)$, with the form,

$$F(t; t_0, \beta, \omega, F_0, B) = F_0 A[x(t; t_0, \beta, \omega)] + B, \quad (3.1)$$

where F_0 is the unlensed flux, and B is the light from any additional unlensed sources that are not resolved. The flux from the satellite can also be described in this manner, by five additional parameters $a'_i = (t'_0, \beta', \omega', F'_0, B')$. Using measurements simulated by our Monte Carlo method, we then fit the parameters by minimizing χ^2 . By differentiating χ^2 in the neighborhood of the solution, one can obtain c_{ij} , the covariance matrix of the a_i for both the Earth and the satellite.

We assume that the Earth and satellite have the same filters, implying that $F_0 = F'_0$ and $B = B'$. Each of these constraints can be written $\sum_{i=1}^{10} \alpha_i a_i = 0$, where a_i are now the ten parameters for the Earth and the satellite, and α_i are the constraint coefficients. The constraint coefficients for $F_0 = F'_0$ are $\alpha_i = (0, 0, 0, 1, 0, 0, 0, 0, -1, 0)$. We impose these constraints on the 10×10 covariance matrix c_{ij} , forming a new matrix \tilde{c}_{ij} ,

$$\tilde{c}_{ij} = c_{ij} - \frac{\sum_{l=1, k}^{10} c_{il} \alpha_l c_{jk} \alpha_k}{\sum_{m, n=1}^{10} c_{mn} \alpha_m \alpha_n}. \quad (3.2)$$

Neglecting the relative Earth-satellite motion, we find that there is a two-fold

degeneracy in the magnitude $|\Delta\beta| = \Delta\beta_{\pm}$, and another two-fold degeneracy in the sign. Thus there are four possible solutions, $\pm\Delta\beta_{\pm}$. In our simulations, we know the true solution, which for the illustrations given here we take to be $+\Delta\beta_-$ or $(-+)$ for short. However, we initially assume that only the magnitudes of β and β' are known, thus making all four possible values of $\Delta\beta$ equally probable. We use the constrained covariance matrix, \tilde{c}_{ij} , to form a new covariance matrix of the quantities $a_i = (\Delta t, \Delta\beta, \Delta\omega)$; we call this new matrix c_{ij}^{-+} . Due to the fact that there are four possible values of $\Delta\beta$, we form four different matrices $c_{ij}^{\pm\pm}$. We then test to see if the solutions are distinguishable from the true solution, using the constraint imposed by the relative motion of the Earth and the satellite, equations (2.3) – (2.5).

The general form of χ^2 can be written as

$$\chi_{-+}^2 = \frac{(\alpha_2 \delta\beta^{-+})^2}{\sum_{m,n=1}^3 c_{mn}^{-+} \alpha_m \alpha_n}, \quad (3.3)$$

where the α_i 's are the coefficients from the constraint condition, and $\delta\beta^{-+}$ is the difference between the true and trial values of $\Delta\beta$. Because χ^2 is a strong function of the phase of the orbit, it is not possible to give χ^2 in a simple form. It is illuminating, however, to examine the form of χ^2 at the values of ψ for which it is at maximum and minimum. For $\psi = (90^\circ, 270^\circ)$, the constraint coefficients are:

$$\alpha_i = (0, \Omega_{\oplus} \cos \alpha, 1) \quad (3.4)$$

and for $\psi = (0, 180^\circ)$,

$$\alpha_i = (0, \Omega_{\oplus}, \cos \alpha). \quad (3.5)$$

We define $q = (\sigma_{\omega}/\sigma_{\beta} t_e \Omega_{\oplus})$, where $\sigma_{\omega} = c_{33}^{1/2} t_e$, and $\sigma_{\beta} = c_{22}^{1/2}$. Using these expressions, and assuming (as is generally the case), that the off-diagonal covariances ($c_{ij}, i \neq j$) are small, the equation for χ^2 can be written for each case as,

$$\begin{aligned}\chi_{min}^2 &= \chi^2(90^\circ, 270^\circ) = \frac{\delta\beta/\sigma_\beta}{1 + (q/\cos\alpha)^2} \\ \chi_{max}^2 &= \chi^2(0, 180^\circ) = \frac{\delta\beta/\sigma_\beta}{1 + (q\cos\alpha)^2}\end{aligned}\tag{3.6}$$

For typical events, $q \sim 6$ for the $\pm\Delta\beta_-$ solutions; this value is roughly independent of ψ .

Note that $\chi_{min}^2/\chi_{max}^2 \sim (\cos\alpha/q)^2$ (for typical time scales). Thus for observations toward the bulge, $\alpha \simeq 84^\circ$, χ^2 can vary by a factor of $10^2 - 10^4$ over the course of the orbit.

We calculate the χ^2 for all four solutions, and consider only those solutions for which $\chi^2 \leq 9$. We then calculate the intrinsic error for these allowed solutions. The fractional error in the scalar solution can be approximated by $\langle(\delta\Delta x)^2\rangle^{1/2}/\Delta x$, where again $\Delta\mathbf{x} \equiv (\omega\Delta t, \Delta\beta) = (a_1, a_2)$, and $\Delta x = |\Delta\mathbf{x}|$. Using the analog of equation (3.2),

$$\tilde{c}_{ij}^{-+} = c_{ij}^{-+} - \frac{\sum_{l=1,k}^3 c_{il}\alpha_l c_{jk}\alpha_k}{\sum_{m,n=1}^3 c_{mn}\alpha_m\alpha_n},\tag{3.7}$$

we apply the constraint (2.3) to c^{-+} to form \tilde{c}^{-+} , where α_i is now given by equation (2.5), and $a_i = (\Delta t, \Delta\beta, \Delta\omega)$. In terms of \tilde{c}_{ij}^{-+} , the fractional error becomes

$$\frac{\langle(\delta\Delta x)^2\rangle^{1/2}}{\Delta x} = \frac{(\sum_{i,j=1}^2 \tilde{c}_{ij}^{-+} a_i a_j)^{1/2}}{(a_1)^2 + (a_2)^2}.\tag{3.8}$$

From this we can see that as the quantities (a_1, a_2) become small, the fractional error in the solutions rise. Recall that for $\psi \sim 0$, the projected Earth-satellite separation is small (relative to the true separation), and therefore Δx is small. Thus the intrinsic errors in the solutions become more important near $\psi = 0$.

We approximate the fractional error in the vector solution by $\langle(\delta\Delta\mathbf{x})^2\rangle^{1/2}/\Delta x$.

This can be written as,

$$\frac{\langle(\delta\Delta\mathbf{x})^2\rangle^{1/2}}{\Delta x} = \left[\frac{\tilde{c}_{11}^{-+} + 2\tilde{c}_{12}^{-+} + \tilde{c}_{22}^{-+}}{(a_1)^2 + (a_2)^2} \right]. \quad (3.9)$$

4. Bulge and Disk Models

In order to calculate the DBF using the Monte Carlo simulation, we adopt appropriate models for the velocity and density distributions of the disk and bulge of the Milky Way.

For the density distributions, we choose a Bahcall model for the disk. For the bulge, we adopt a ‘revised’ COBE model. This model uses a barred bulge density distribution for the outer parts of the bulge ($r > 0.7$ kpc) and a Kent model for the inner part of the bulge. For a more detailed description, see Table 3 from Han & Gould (1995).

We assume the velocity distributions to be Gaussian, with mean velocity \bar{v} , and velocity dispersion σ . For the disk, we use $(\bar{v}_x, \bar{v}_y, \bar{v}_z) = (0, 220, 0)$; with dispersions of $(\sigma_x, \sigma_y, \sigma_z) = (40, 30, 20)$ km s⁻¹. For the bulge, $(\bar{v}_x, \bar{v}_y, \bar{v}_z) = (0, 0, 0)$, while $(\sigma_x, \sigma_y, \sigma_z) = (110, 82.5, 66.3)$ km s⁻¹. The motion of the Sun is also taken into account, and is $(v_x, v_y, v_z) = (9, 231, 16)$ km s⁻¹ (Mihalas & Binney 1981).

There are two distinct types of events that are seen towards the bulge. These are bulge-bulge events, where a bulge star is being lensed by bulge lens, and disk-bulge events, where a bulge star is being lensed by a disk lens. These two situations produce dissimilar events, and we therefore consider them separately.

For disk-bulge events, the position of the source star, d_{os} is confined to a relatively narrow range as compared to the range of possible values for d_{ol} . Thus we can approximate the location of the source stars as being fixed at the galactocentric radius, $R_0 = 8$ kpc. The frequency of lensing events scales as $\rho(r_1)r_{ev} \propto \rho(r_1)[z(1-z)]^{1/2}v$, where v is the transverse velocity of the lens, r_1 is the distance of the lens from the galactic center (for lines of sight near the galactic center,

$r_l \simeq d_{ls}$), and $\rho(r_l)$ is the mass density at r_l . Thus to simulate an event, we draw the distance to the lens randomly from the probability distribution $\rho(r_l)[z(1-z)]^{1/2}$. The velocities of the lens and the source are then drawn randomly according to the parameters described above, and the transverse velocity calculated. We weight the DBF by the transverse speed in order to include its effect on the event rate.

For bulge-bulge events, the frequency of lensing events depends on the mass density at the position of the source, the mass density at the position of the lens, the size of the Einstein ring, and the transverse velocity of the lens. In addition, as the distance from the observer increases, the volume element along the line of sight also increases, and therefore so does the total number of stars. Thus the event rate scales as $\rho(r_s)\rho(r_l)r_e d_{os}^2 v$. Here r_s is the distance of the source from the galactic center, and d_{os}^2 provides the contribution due to the increasing volume element. Thus, the source-lens pair position (d_{os}, d_{ol}) is drawn randomly from the distribution $\rho(r_s)\rho(r_l)[z(1-z)]^{1/2} d_{os}^2$. The resulting DBF is weighted by the transverse velocity, as above.

5. Monte Carlo

For the simulation, we assume that the observations begin when the source enters the Einstein ring radius as seen from the Earth. The observations continue until the source-lens separation is $\geq 3r_e$ as seen from both the Earth and the satellite. The impact parameter, β , is either fixed, or chosen randomly in the range $0 < \beta < 0.7$. This range of β is consistent with that of observed microlensing events. Those events for which the time of maximum magnification for the satellite has already passed when the observations begin, that is, $(1 - \beta^2)^{1/2} < \omega \Delta t$, are considered unresolvable. Those events for which $\beta' > 1.5$ are also considered unresolvable.

The four possible solutions are considered separately, and the χ^2 calculated for each. Those solutions for which $\chi^2 > 9$ are distinguishable from the true solution, and are therefore unallowed. We then determine if the allowed solutions

are sufficiently similar that it is unimportant to break the degeneracy, and if the fractional errors in the solutions are intolerably large. The scalar difference between the solutions is given by,

$$\delta(\Delta x) = |\Delta x|_{\text{allowed}} - |\Delta x|_{\text{true}}, \quad (5.1)$$

whereas the vector difference is given by,

$$\delta(\Delta \mathbf{x}) = |\Delta \mathbf{x}_{\text{allowed}} - \Delta \mathbf{x}_{\text{true}}|. \quad (5.2)$$

If the difference between all allowed solutions and the true solution is less than 20% of the true solution, and if the fractional error in Δx of each allowed solution is less than 10%, we consider that the degeneracy is broken. For each set of parameters, the Monte Carlo simulation was run 5000 times, resulting in errors of $< 1\%$.

6. Observational Considerations

Because the bulge is located at ecliptic angle $\alpha \sim 90^\circ$, there will be times of the year that observations will be impossible, due to the position of the Sun. To quantify this effect, we define an allowed range of the ecliptic longitude, Λ , for the Earth and the satellite. When the position of the Earth or the satellite is within this range, observations are considered impossible. The full width of this range is chosen to be 90° (3 months) for the Earth, and 60° (2 months) for the satellite. In our simulations, we consider lines of sight towards the bulge, for which $\Lambda = 270^\circ$. The forbidden ranges for the Earth and satellite are then,

$$\begin{aligned} 90^\circ - 45^\circ &\leq \Lambda_E \leq 90^\circ + 45^\circ \\ 90^\circ - 30^\circ &\leq \Lambda_S \leq 90^\circ + 30^\circ. \end{aligned} \quad (6.1)$$

Note that $\Lambda = 0$ is the vernal equinox. The time of the year when either the Earth or the satellite is within the forbidden range is dependent on the Earth-satellite

separation, d_{sat} . For $d_{\text{sat}} \leq 75^\circ$, the forbidden ranges of the Earth and satellite overlap. Conversely, for $d_{\text{sat}} \geq 75^\circ$, the forbidden ranges are separated by a gap of $\Delta\Lambda = d_{\text{sat}} - 75^\circ$. Thus values of $d_{\text{sat}} \geq 75^\circ$ are somewhat less desirable due to the fact that the times of year when observations are possible are separated into two ranges, thereby increasing the probability that the observations of an event will be foreshortened due to the Earth or the satellite moving behind the Sun. We will consider this issue more fully in § 7.1, when we discuss the optimal Earth-satellite separation.

7. Results

There are eight parameters that affect the degeneracy breaking fraction; α , the angle between the source and the south ecliptic pole; ψ , which is related to the phase of the orbit; σ_E and σ_S , the photometric precisions of the Earth and satellite observations, respectively; β , the impact parameter as seen from the Earth; d_{sat} , the Earth-satellite separation distance; M , the mass of the lens; N_{meas} , the number of measurements per Einstein ring crossing time.

For all of the parameters (neglecting ψ for the moment), we choose typical values that we consider to be realistic. These values are used in all simulations unless varied explicitly. A value of $N_{\text{meas}} = 20$ corresponds to frequency of measurements in the range of 0.5 to 4.0 days for typical events. We choose $(\sigma_E, \sigma_S) = (1\%, 2\%)$ as our photometric precision. The photometric precision obviously depends on the magnitude of the source star; these are typical values of photometric precision for giant sources. We choose $M = 0.3M_\odot$ as a representative mass of lenses for observations towards the bulge. The default Earth-satellite separation is $d_{\text{sat}} = 60^\circ$ (2 months). The maximum impact parameter is set at $\beta_{\text{max}} = 0.7$. For Baade's window, $\alpha = 84^\circ$.

Observations towards the bulge are unique in that they are a strong function of the time of year, as discussed above. Due to this intrinsic dependence of the DBF on ψ , we include ψ as a free parameter in all further calculations.

In order to elucidate the effect of the time of the year on the DBF, we present in Figure 2 the DBF against ψ for our fiducial parameters. Included in Figure 2 are the results for both the disk-bulge and bulge-bulge cases. Also included is the DBF against ψ for disk-bulge events assuming a fractional difference threshold of 5% (see § 2.3). Within the limits of the Monte Carlo errors, we find that in the range $0 \leq \psi \leq 180^\circ$ the curve is equivalent to that for the range $180^\circ \leq \psi \leq 360^\circ$. We utilize this symmetry by restricting the range of ψ in further calculations to $0 \leq \psi \leq 180^\circ$. There is, however, a slight asymmetry around $\psi = 90^\circ$ (and similarly around $\psi = 270^\circ$). For the speed degeneracy, this asymmetry makes no significant contribution, and we disregard it. We will consider this effect more fully in § 8, where we discuss the velocity degeneracy. For $\psi \sim 0, 180^\circ$, we see from equation (2.2) that the projected Earth-satellite velocity is at a maximum, and as a result the constraint given in equation (2.1) is very effective in distinguishing between the possible solutions. The projected Earth-satellite separation is at a minimum, however, driving up the fractional errors in the solutions. Thus near $\psi \sim 0, 180^\circ$, the DBF is dominated by the intrinsic errors. As ψ increases, the projected Earth-satellite separation increases, and thus the intrinsic errors decrease. The projected Earth-satellite velocity decreases as ψ increases, and as a result the constraint becomes less effective in distinguishing between the degenerate solutions. For $\psi \simeq 20^\circ$ the DBF is at a maximum; the constraint still distinguishes between the solutions for a majority of the events, while the intrinsic errors are typically $\leq 10\%$. When $\psi = 90^\circ$, the projected Earth-satellite separation is equal to the true Earth-satellite separation, and the intrinsic errors are typically $\leq 5\%$. The projected Earth-satellite velocity is at a minimum at $\psi = 90^\circ$, and the constraint distinguishes poorly among the solutions (as compared to $\psi \sim 0$). Thus, at $\psi = 90^\circ$, the DBF is dominated by the difficulty in distinguishing between the individual solutions. The analysis of the DBF curve in the range $0 \leq \psi \leq 90^\circ$ is identical to that for the rest of the orbit.

The analysis of bulge-bulge events is exactly the same as for disk-bulge events. We can understand how disk-bulge and bulge-bulge events differ by considering the

typical size of the projected Einstein ring in each case. For disk-bulge events, the median value for the distance to lens is $d_{ol} \sim 5$ kpc, and the distance to the source is $d_{os} = 8$ kpc, thus, from equations (1.2) and (1.4), we find that, for disk lenses, $\tilde{r}_e \simeq 6.0\text{AU}(M/0.3M_\odot)^{1/2}$. For bulge-bulge events, $d_{ol} \sim 7$ kpc, $d_{os} \sim 9$ kpc, so that $\tilde{r}_e \simeq 9.0\text{AU}(M/0.3M_\odot)^{1/2}$. Therefore the typical size of the projected Einstein rings will be larger for bulge-bulge events by a factor of ~ 1.5 . This will affect the value of the DBF in two distinct ways. For phases of the orbit such that $\psi \sim 0$, where intrinsic errors dominate, the DBF for bulge-bulge events will be smaller than that for disk-bulge events, due to the larger typical values of \tilde{r}_e (and therefore larger fractional errors). For phases of the orbit such that $\psi \sim 90^\circ$, we expect that the DBF for bulge-bulge events will be, in general, higher than the corresponding DBF for disk-bulge events, due to the fact that the degenerate $\Delta\beta$ solutions are better separated in the case of the bulge-bulge events than those for disk-bulge events.

For disk-bulge events, we find that for our fiducial parameters, it is possible to resolve $> 87\%$ of the events during most times of the orbit, and $> 70\%$ of the events over the entire orbit. For bulge-bulge events, we find values of $> 90\%$ for most of the orbit and $> 60\%$ for the entire orbit.

Figure 3 represents the DBF as a function of ψ and β for disk-bulge events. For this figure, β is not randomly chosen, but rather held fixed for each point in the curve. Contrary to the results for the LMC (Boutreux & Gould 1996), where it was found that events with $\beta \geq 0.7$ are much harder to resolve, there is no one value of β for which the DBF drops below a certain value. In fact, for $\psi = 90^\circ$, even those events for which $\beta \sim 0.9$ are resolvable 80% of the time, whereas less than 20% of these events are resolvable when $\psi = 10^\circ$. In other simulations, we choose β randomly between $0 \leq \beta \leq 0.7$ because the majority of events seen so far have values of β that are in this range, but we emphasize that, under the proper conditions, even those events that have $\beta > 0.7$ may still be resolvable.

Figure 4 represents the DBF as a function of ψ and M for disk-bulge events.

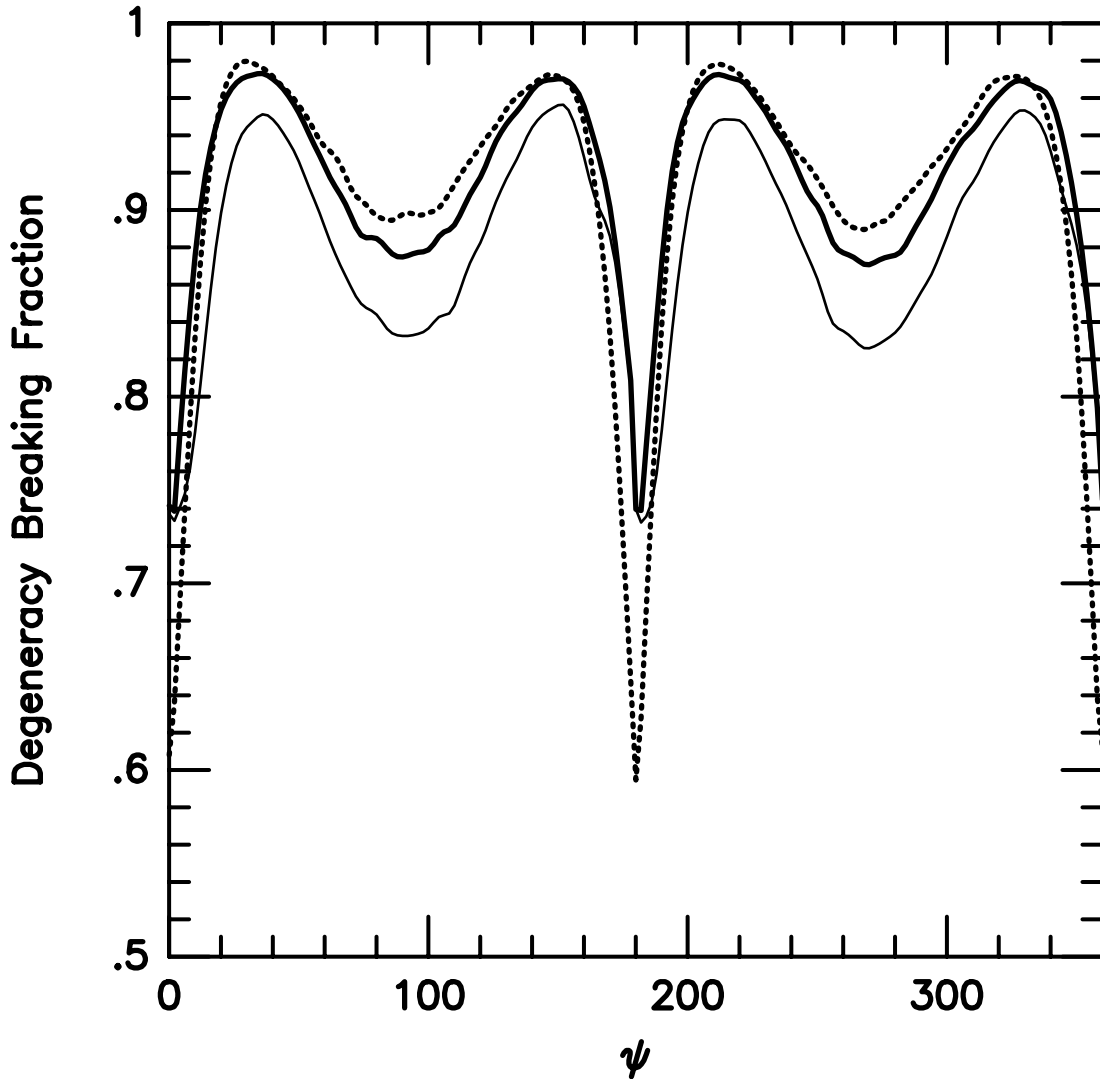


Figure 2. Degeneracy Breaking Fraction (DBF) as a function of ψ for disk-bulge events (solid bold curve) and bulge-bulge events (dashed curve). All other parameters are fixed at $n_{obs} = 20$, $(\sigma_E, \sigma_S) = (1\%, 2\%)$, $M = 0.3M_\odot$, $d_{sat} = 60^\circ$, $\beta_{max} = 0.7$, and $\alpha = 84^\circ$. The DBF is the fraction of events for which the allowed solutions differ by $< 20\%$ and each of these has intrinsic error $< 10\%$. The lower solid curve is the DBF as a function of ψ when allowed solutions differ by $< 5\%$, and each has intrinsic error $< 10\%$.

For the mass, we focus on the range $0.01M_\odot - 1M_\odot$; this corresponds to the best estimate of the range of masses for events already observed. For our fiducial value, $M = 0.3M_\odot$, the DBF is $\sim 90\%$ for the majority of the orbit. For disk-bulge

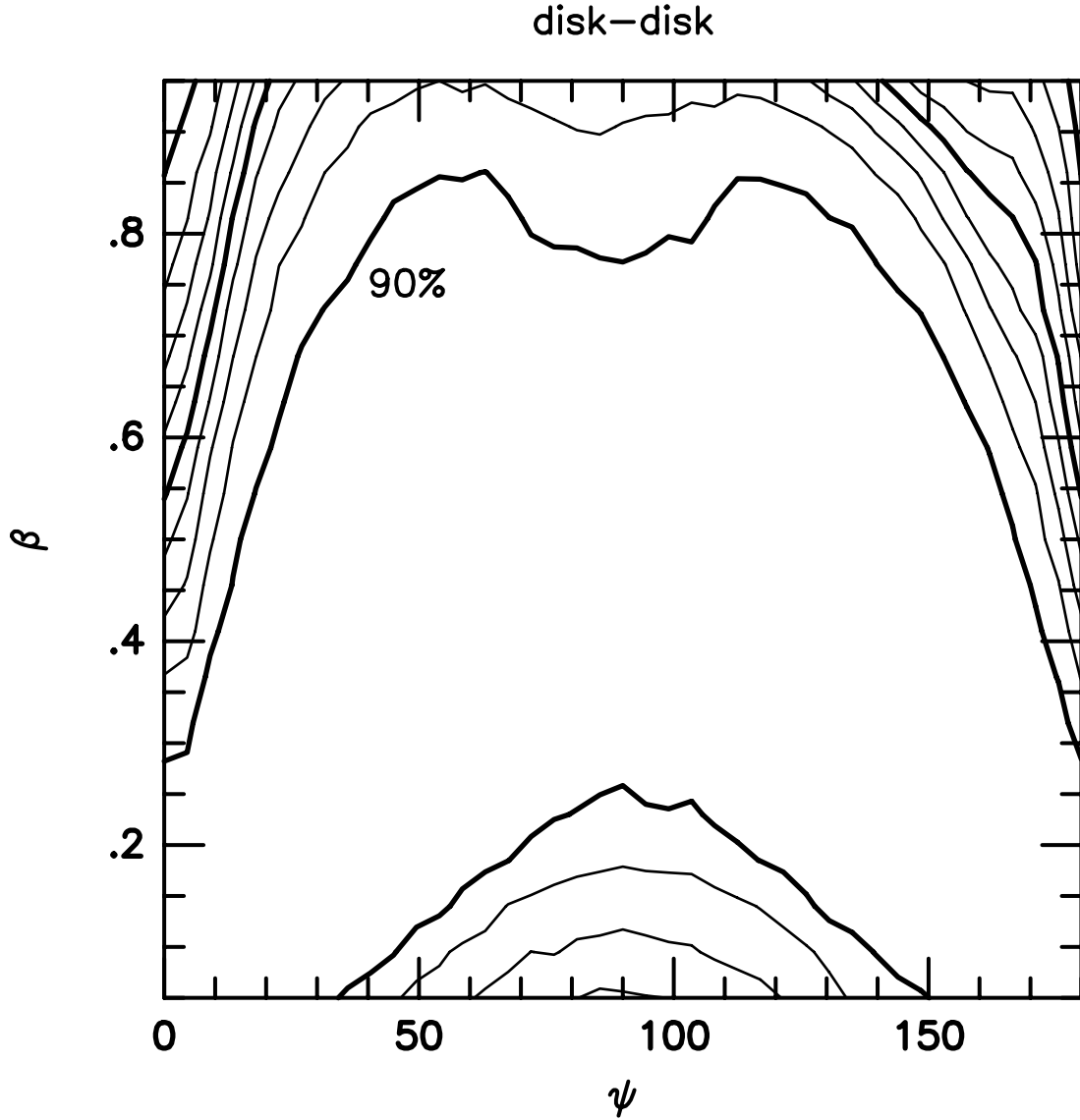


Figure 3. DBF as a function of ψ and β for disk-bulge events. The labeled bold contour represents a DBF of 90%. Other bold contours represent DBFs of 50% and 10%. Intermediate contours are spaced at intervals of 10%. All other parameters are held fixed at our fiducial parameters, as in Fig. 2.

events, the projected Einstein ring radius is $\tilde{r}_e \simeq 6.0\text{AU}(M/0.3M_\odot)^{1/2}$. Consider first phases of the orbit for which $\psi \sim 0$, where the fractional errors dominate the behavior of the DBF. For these values of ψ (and $R \sim 1\text{AU}$), the projected Earth-satellite separation is $r \sim 0.1\text{AU}$. The fractional errors become important

when $\Delta x \ll 1$. A quick calculation shows that, for masses greater than $M \geq 0.1M_\odot$, the magnitude of the vector displacement is $\Delta x = r/\tilde{r}_e < 0.1$, and thus the fractional errors begin to dominate, thereby lowering the DBF. For masses $M \leq 0.03M_\odot$, $\Delta x = r/\tilde{r}_e \sim 1$, and thus the fractional errors are unimportant, and the DBF is $> 90\%$. Consider now phases of the orbit for which $\psi \sim 90^\circ$. For the range of masses considered here, $\Delta x \geq 1$, and thus the fractional errors are never large. Considering increasingly smaller masses, we find that more of the events are unresolvable, due to the fact that the projected Earth-satellite separation, r , becomes increasingly larger than the Einstein ring radius, \tilde{r}_e , and the event as seen from the satellite will more frequently fall outside of the Einstein ring. Thus the DBF drops rapidly from 90% to 40% from $M = 0.3M_\odot$ to $M = 0.03M_\odot$.

Figure 5 represents the DBF as a function of ψ and B , the ecliptic latitude ($B = \alpha - 90^\circ$), for disk-bulge events. For this figure, we hold the ecliptic longitude fixed at $\Lambda = 270^\circ$, and vary B in the range $-10^\circ \leq B \leq 10^\circ$. In galactic coordinates, this corresponds to the range $(l, b) = (-2^\circ, -5^\circ) - (16^\circ, 4^\circ)$. For Baade's window, $B = -6^\circ$, the DBF is greater than 90% for the entire orbit. Note that for $B = 0$, it is impossible to break the degeneracy. This is due to the fact that, at $B = 0$, the constraint given in equation (2.1) becomes $\sum_{i=1}^3 \alpha_i a_i = \Delta\omega + \Omega_\oplus \omega \Delta t \cot \psi = 0$, and thus does not constrain the value of $\Delta\beta$ at all. Similarly, for small values of $|B|$, the value of $\Delta\beta$ is poorly constrained. Thus, there is range of ecliptic latitude, $|B| < 1^\circ$, where the DBF is less than 40% for a majority of the orbit; this range should be avoided when making observations. Lines of sight where $|B| > 2^\circ$ are optimal.

Figure 6 represents the DBF as a function of ψ and d_{sat} , the Earth-satellite separation, for disk-bulge events. Also shown is the range of ψ for which observations are impossible due to the position of the Sun. This range is a function of d_{sat} ; thus by considering simultaneously how this range and the DBF vary as function of d_{sat} , we can find an optimal Earth-satellite separation. For $d_{\text{sat}} \leq 30^\circ$, the range where observations are impossible is smallest ($\sim 90^\circ$), but the DBF is never greater than 80%. For $d_{\text{sat}} = 60^\circ$, the observationally forbidden range is

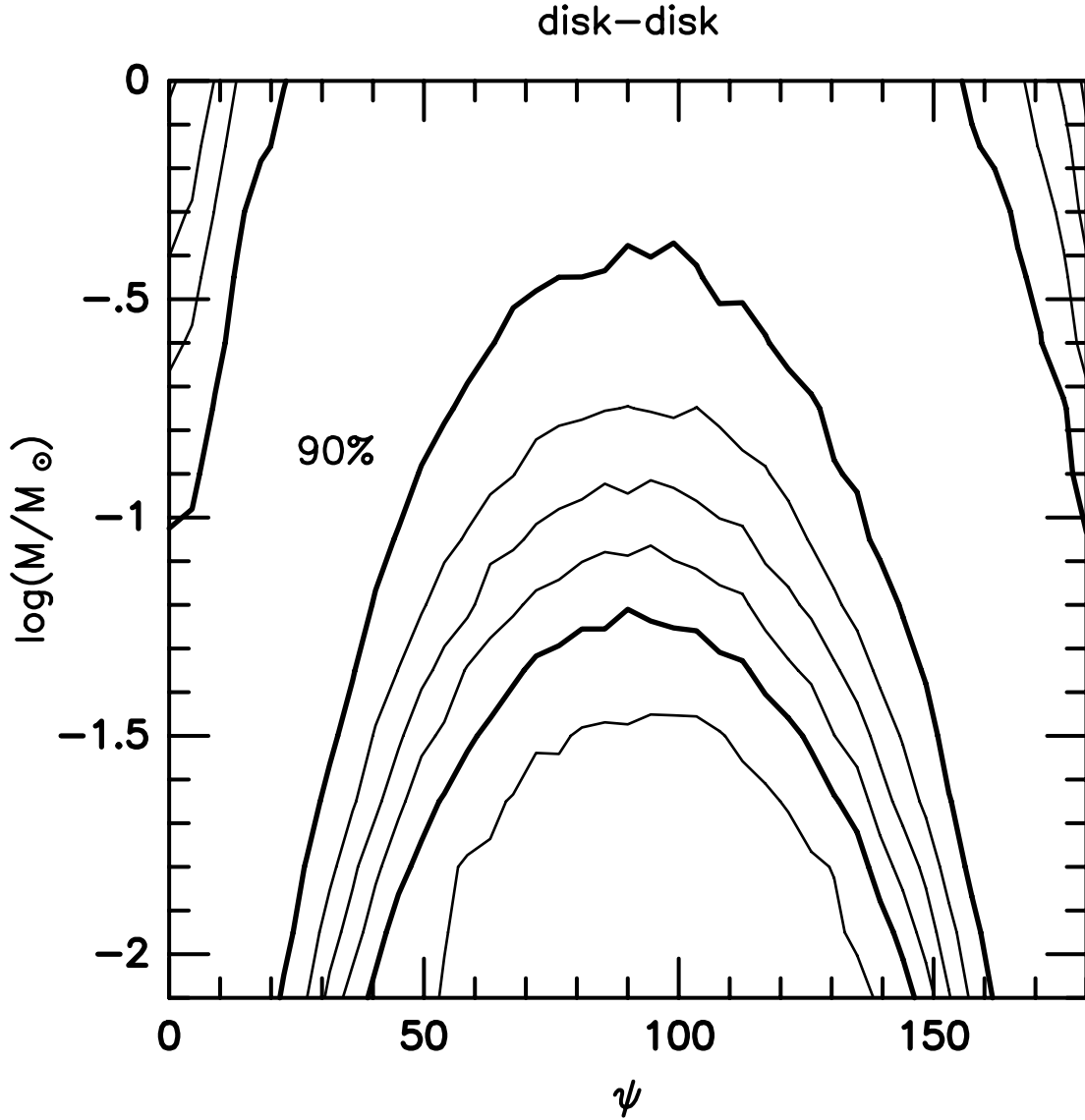


Figure 4. DBF as a function of ψ and $\log M/M_{\odot}$ for disk-bulge events. Contours are the same as those in Fig. 3.

only slightly larger ($\sim 130^{\circ}$), and the DBF is greater than 90% for the majority of the orbit. For $d_{\text{sat}} > 75^{\circ}$, the forbidden ranges for the Earth and the satellite begin to diverge, and the times of the orbit where observations are possible become separated. Thus, although the DBF continues to improve as d_{sat} increases, there is an increased likelihood for these ranges that an observation will be foreshortened

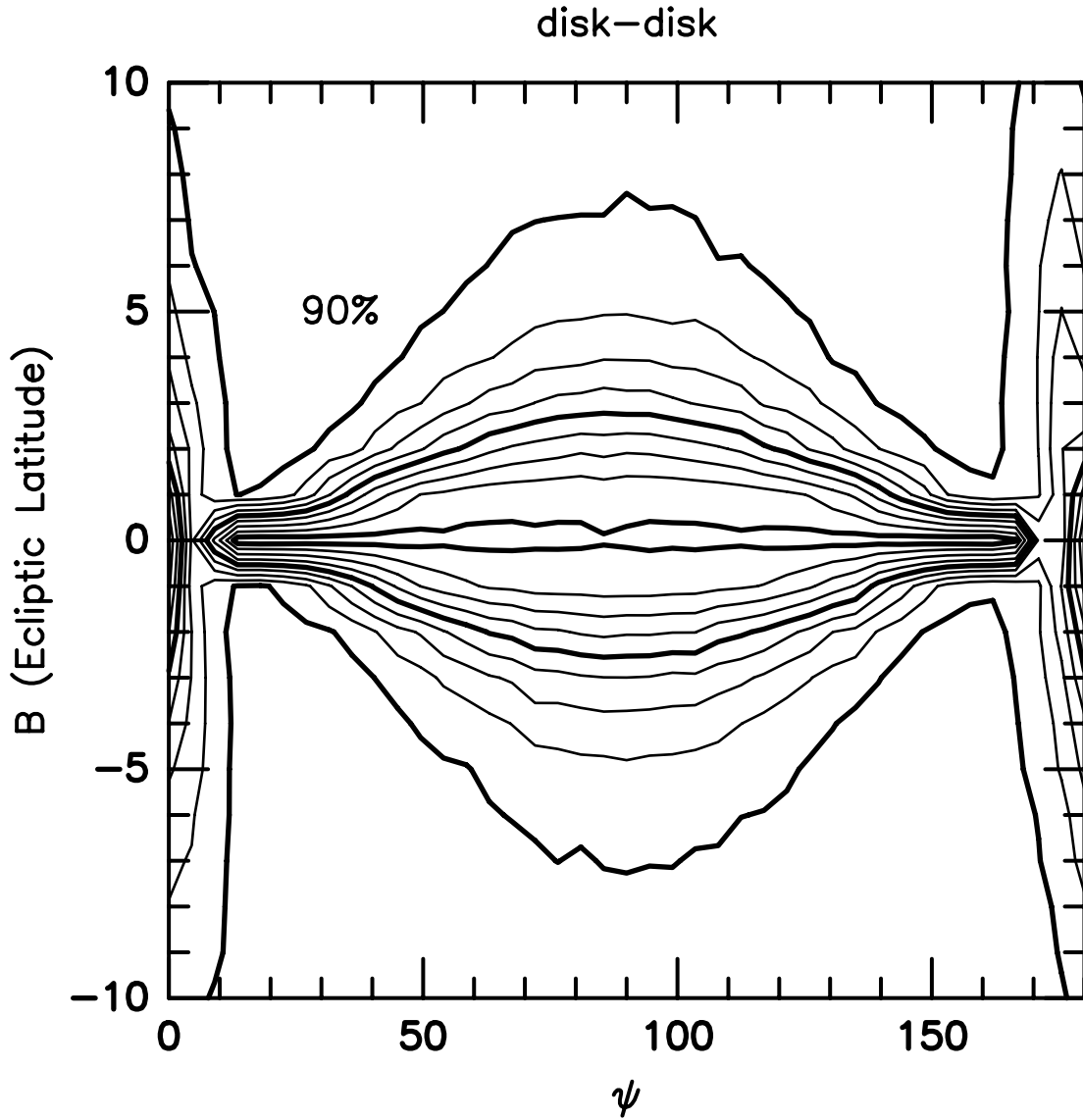


Figure 5. DBF as a function of ψ and B for disk-bulge events. Contours are the same as those in Fig. 3.

due to the Earth or the satellite moving behind the Sun. We consider $20^\circ - 75^\circ$ to be the optimal range for the Earth-satellite separation. For $d_{\text{sat}} < 20^\circ$, the DBF is unacceptably low.

We also considered the dependence of the DBF on the parameters β , M , B, and d_{sat} for bulge-bulge events. We find the results to be almost identical to those

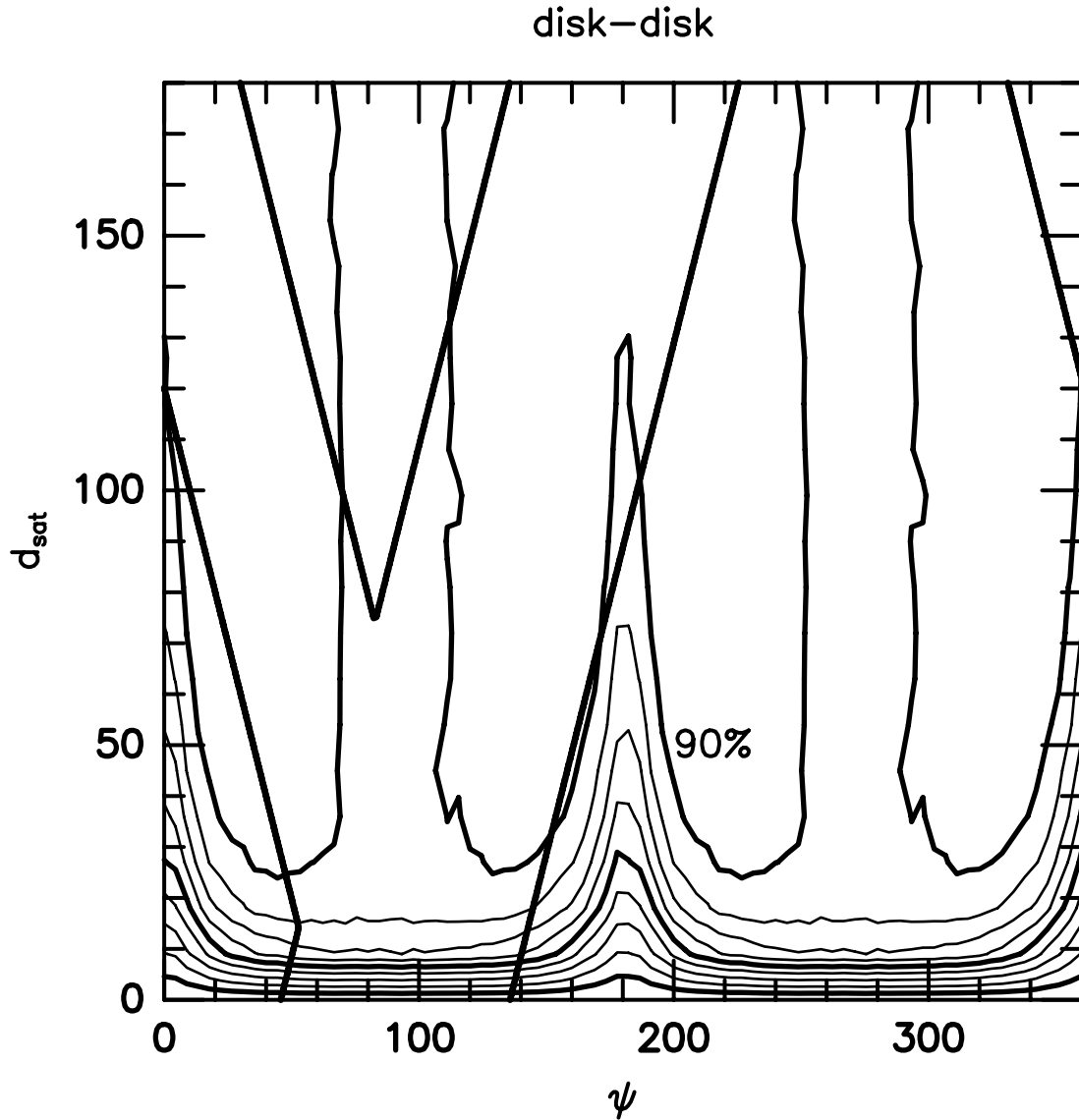


Figure 6. DBF as a function of ψ and d_{sat} for disk-bulge events. The y-shaped area of the graph between the heavy lines represents those range of ψ for each value of d_{sat} where observations are impossible due to the position of the Sun. The other contours are the same as those in Fig. 3.

for disk-bulge events, with variations of at most $\sim 10\%$, when the phase of the orbit is $\psi \sim 0$ or 180° , but typically the variations are much smaller. For reasons discussed above, the DBF is, in general, somewhat higher when $\psi \sim 90^\circ$, and somewhat lower when $\psi \sim 0$ for bulge-bulge events. As with disk-bulge events, we

find that there is no natural cutoff value for β ; for our fiducial value of $M = 0.3M_{\odot}$, the DBF is $\sim 90\%$ for the majority of the orbit; for Baade’s window, $B = -6^{\circ}$, the DBF is greater than 90% for the majority of the orbit; and the optimal range of d_{sat} is $20^{\circ} - 75^{\circ}$. Overall, the differences between bulge-bulge and disk-bulge events are minor, and will not significantly affect the observations.

8. The Velocity Degeneracy

In the previous section, we discussed the observational requirements of a satellite to break the two-fold degeneracy in the projected speed, \tilde{v} . While measuring the projected speed is helpful in distinguishing between component populations, a measurement of the projected velocity, $\tilde{\mathbf{v}}$, would provide a more conclusive distinction.

In this section we present the results for breaking the four-fold velocity degeneracy, adopting the fiducial parameters used in the previous section: $N_{\text{meas}} = 20$, $(\sigma_E, \sigma_S) = (1\%, 2\%)$, $M = 0.3M_{\odot}$, $d_{\text{sat}} = 60^{\circ}$ (2 months), $\beta_{\text{max}} = 0.7$, and $\alpha = 84^{\circ}$. We calculate the difference between the allowed solutions using equation (5.2), and the fractional error in each allowed solution using equation (3.9). As in the previous section, if the intrinsic errors in all allowed solutions is $< 10\%$, and if the difference between the allowed solutions is $< 20\%$ of the true solution, we consider the degeneracy to be broken. Here we present the results for both disk-bulge and bulge-bulge type events.

Figure 7 represents the vector DBF as a function of ψ for disk-bulge events and bulge-bulge events. The scalar DBF is also shown for comparison. We find that for disk-bulge events the DBF is greater than $\sim 40\%$ for the entire orbit, and greater than $\sim 55\%$ for about half the orbit. We find that for bulge-bulge events the vector DBF is $\gtrsim 30\%$ over the entire orbit, and $\gtrsim 40\%$ over half the orbit. In general, the analysis of the vector DBF curve is the same as that for scalar DBF curve: there are minima at $\psi = 0$ and 180° where the intrinsic errors dominate the DBF, and a minimum at $\psi = 90^{\circ}$ where the ability of the constraint

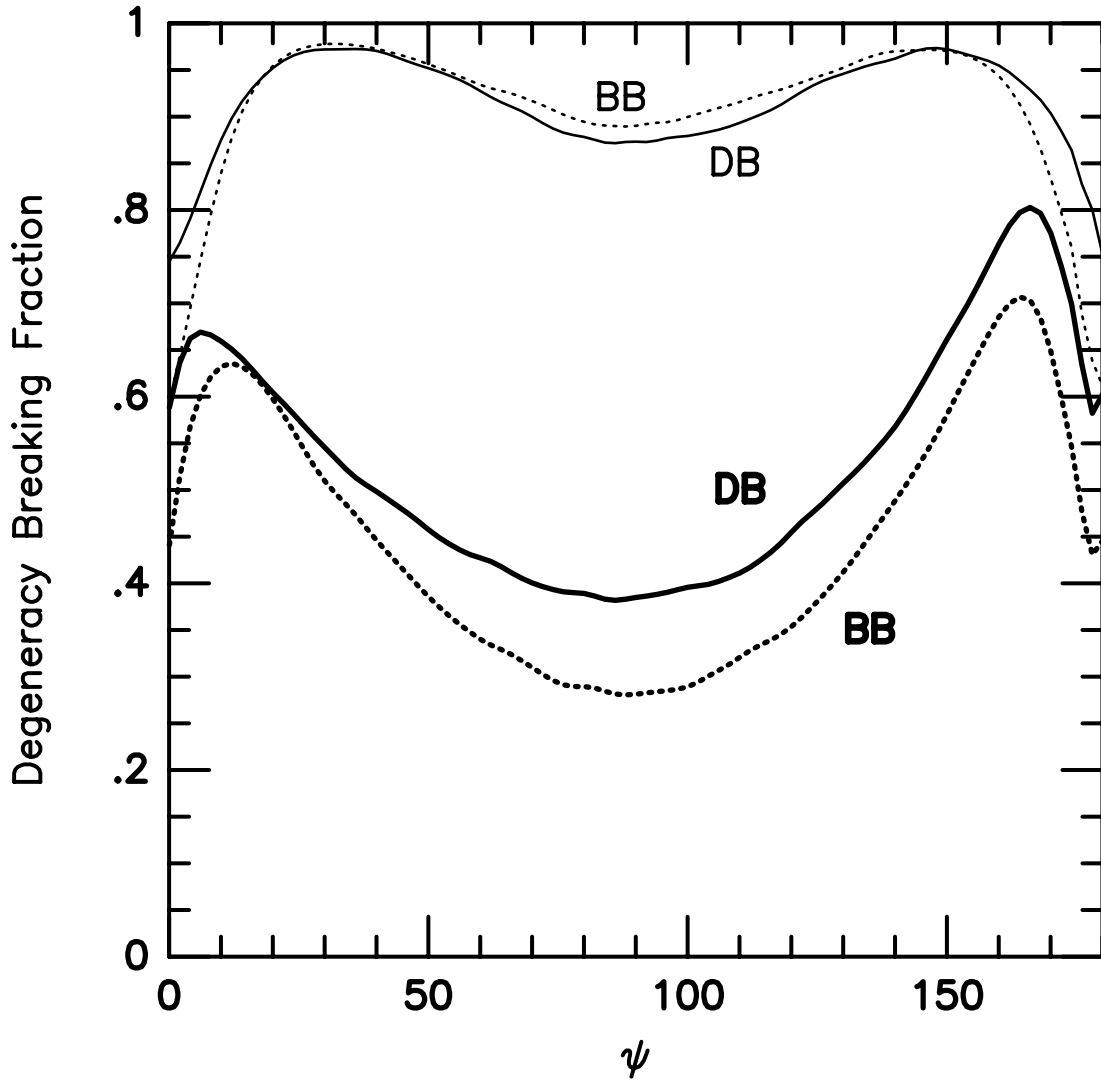


Figure 7. Vector DBF as a function of ψ for disk-bulge events (bold solid curve) and for bulge-bulge events (bold dashed curve). Also shown is the corresponding scalar DBF. All other parameters are fixed at $n_{obs} = 20$, $(\sigma_E, \sigma_S) = (1\%, 2\%)$, $M = 0.3M_\odot$, $d_{sat} = 60^\circ$, $\beta_{max} = 0.7$, and $\alpha = 84^\circ$.

to distinguish between the degenerate solutions dominates the DBF. There are two unique features of the vector DBF, however. The first is that the minimum value of the DBF occurs at $\psi \sim 90^\circ$, where the limiting factor is the ability to distinguish between the solutions. In the scalar case, distinguishing between the

$\pm\Delta\beta_-$ solution is unimportant, due to the fact that these solutions have essentially the same projected speed. To break the vector degeneracy, however, one must distinguish between the $\pm\Delta\beta_-$ solutions, which is often difficult when $\psi \sim 90^\circ$, where the constraint is the least effective. We also find a significant asymmetry in the vector DBF curve around $\psi = 90^\circ$, the largest asymmetry being a difference of $\sim 15\%$ between the DBF at $\psi = 15^\circ$ and 165° . This asymmetry is caused by the fact that lenses in the disk have a preferred direction of motion, and, to a lesser extent, from the motion of the Sun around the galactic center. For a given event, $\Delta\beta \propto \tilde{v}_\perp$, where \tilde{v}_\perp is the component of the transverse velocity perpendicular to the projected Earth-satellite separation, \mathbf{r} . As ψ changes, the direction perpendicular to \mathbf{r} changes with respect to the preferred direction of disk. Thus a preferred direction for $\tilde{\mathbf{v}}$ will translate into an asymmetry in the distribution of values of $\Delta\beta$ around $\psi = 90^\circ$. Specifically, the values of $\Delta\beta$ are typically smaller when $\psi < 90^\circ$ than when $\psi > 90^\circ$. Therefore, because the $\pm\Delta\beta_-$ solutions are, on average, more closely spaced when $\psi < 90^\circ$, the constraint is less likely to distinguish between them, and the DBF is smaller. This asymmetry does not arise in the scalar DBF curve because it is not necessary to distinguish between the $\pm\Delta\beta_-$ solutions. Note the smaller asymmetry around $\psi = 90^\circ$ for bulge-bulge events. This is due to the fact that, in bulge-bulge events, there is no preferred direction of motion of the lens as there is in disk-bulge events.

Acknowledgement: We would like to thank C. Han for making helpful suggestions. This work was supported in part by grant AST 94-20746 from the NSF and by grant NAG5-3111 from NASA.

APPENDIX Generalized Satellite Orbits

For our Monte Carlo simulations, we assumed that the satellite is in an Earth-like orbit, and that both the orbit of the Earth and the orbit of the satellite are circular. In reality, a satellite launched from the Earth will not be in an Earth-like orbit, but will actually be in an elliptical orbit. This implies that the true velocity of the satellite will differ from the assumed velocity for each value of the Earth-satellite separation. In this appendix, we show that, for a reasonably small deviation from a circular orbit, the difference between the true and assumed Earth-satellite velocity will be small, and that therefore our results are sufficiently generic to be applicable to a large class of orbits.

When launched from the Earth, the satellite will have some velocity with respect to the Earth. We assume the direction of the satellite's velocity is parallel to that of the Earth (i.e. the orbit of the satellite is in the plane of the Earth's orbit, and the satellite's perihelion is at the distance of the Earth). That is, $v_{\text{sat}} = v_{\oplus} + \delta v$. We assume that the orbit of the Earth is circular, therefore a non-zero value of δv implies that the satellite will have an elliptical orbit with a period different from that of the Earth's, and it will drift away from the Earth over time. Using Kepler's laws, one finds that the difference between the period of the Earth and the satellite is given by,

$$\frac{\delta P}{P_{\oplus}} = \frac{3\delta v}{v_{\oplus}}. \tag{A.1}$$

In § 8.2, we determined that the optimal Earth-satellite separation was in the range $20^{\circ} - 75^{\circ}$, or $\frac{2}{3}$ month $- 2\frac{1}{2}$ months. We would like the Earth-satellite separation to vary in this range over the course of ~ 3 years. For definiteness, we choose the Earth-satellite separation to be 3 months after 3 years, i.e. $\delta P/P_{\oplus} \sim 1/12$. Thus, from equation (A.1), and using $v_{\oplus} = 30 \text{ km s}^{-1}$ we find $\delta v \sim 0.8 \text{ km s}^{-1}$. The orbit is nearly circular, with an eccentricity of $e = 0.06$.

Using the parameters of the orbit, we can now calculate the difference between the true value of the Earth-satellite velocity and the value used in our simulation

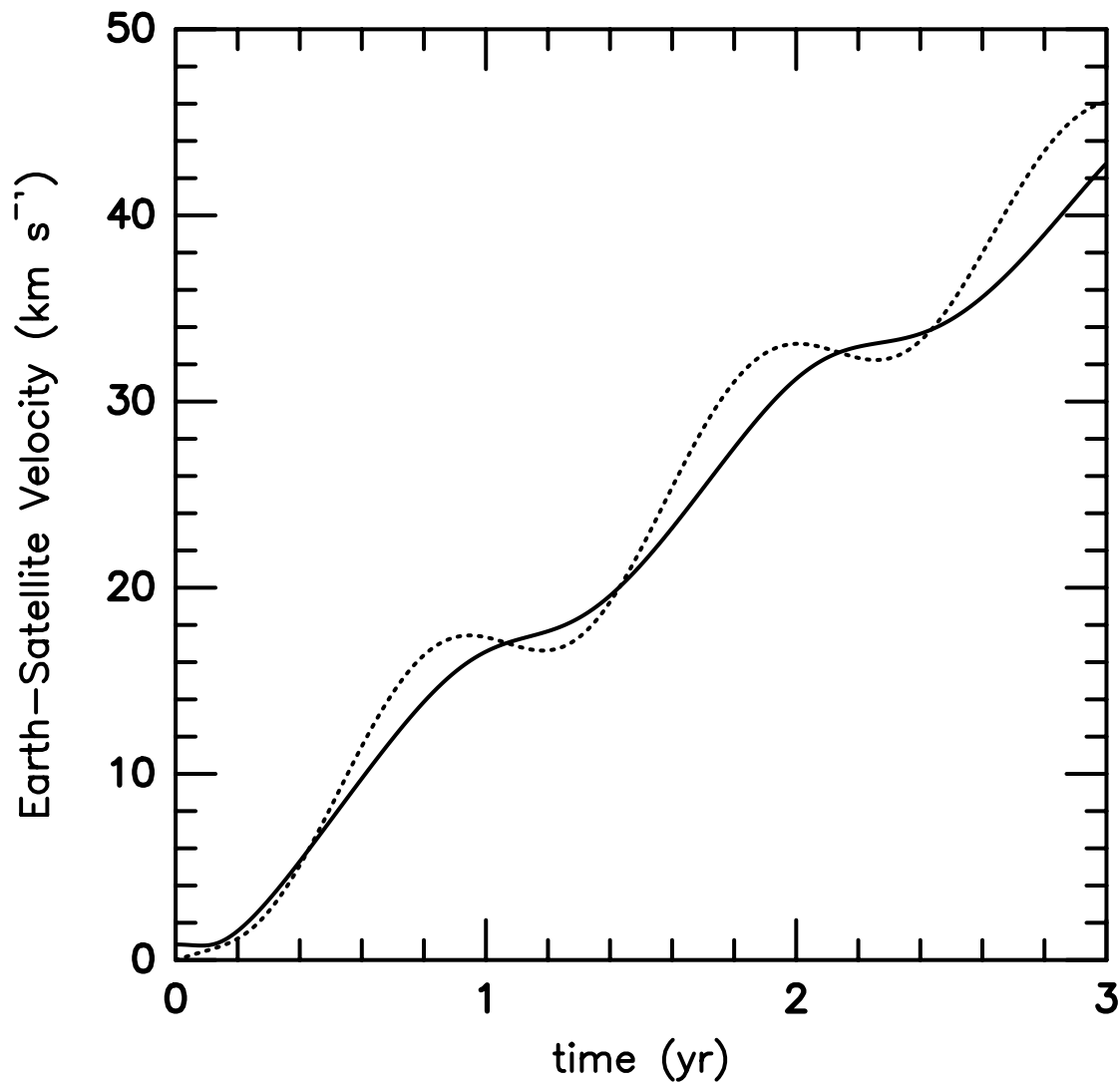


Figure 8. Earth-satellite velocity as a function of time from launch. Shown are the Earth-satellite velocity assuming a circular orbit (dotted line), and the real Earth-satellite velocity (solid line).

(which assumed a circular, Earth-like orbit for the satellite). We set $t = 0$ as the time of launch, and at each point in time, we calculate the true Earth-satellite separation and velocity. We then calculate what the value of the Earth-satellite velocity would be if the satellite were in an Earth-like orbit, separated from the Earth by an amount equal to the true Earth-satellite separation. This corresponds

to the velocity used in our Monte Carlo code. Figure 8 shows the Earth-satellite velocity for both cases in the range $0 \leq t \leq 3$ years. Focusing on $t > 0.5$ year, we find that the true velocity is systematically smaller than the assumed velocity by $\sim 6\%$, but varies from being $\sim 18\%$ smaller to $\sim 6\%$ larger.

Here we have calculated the difference between the true Earth-satellite velocity and that assuming an Earth-like orbit for the satellite. For the purpose of degeneracy breaking, however, it is the projected Earth-satellite velocity that is important. In the case of an elliptical orbit, the magnitude of the projected Earth-satellite velocity is dependent on the time of year in which the satellite is launched. Since we do not know *a priori* when this will be, we cannot find precisely the difference between the true and assumed projected Earth-satellite velocity. This is not strictly necessary, however, since the difference between the projected velocities will be of the same order as the difference between the space velocities. Since the ability to break the degeneracy is roughly proportional to the projected Earth-satellite velocity, we conclude that the error introduced in our simulation by assuming an Earth-like orbit for the satellite is of order the error in the Earth-satellite velocity, $\sim 6\%$.

We conclude that the results obtained in our simulations are applicable to likely satellite orbits. If, however, one would like to consider satellite orbits that are either highly inclined to the Earth's orbit, or highly eccentric, then our results are not applicable. These situations will need to be analyzed individually.

REFERENCES

1. Alcock, C. et al. 1995a, ApJ, 445, 133
2. Alcock, C. et al. 1995b, ApJ, 449, 28
3. Alcock, C. et al. 1995c, ApJ, 454, L125
4. Alcock, C. et al. 1996a, ApJ, submitted (astro-ph=9512145)
5. Alcock, C. et al. 1996b, ApJ, submitted (astro-ph=9606012)
6. Alard, C. 1996, in Proc. IAU Symp. 173, Astrophysical Applications of Gravitational Lensing, ed. C. S. Kochanek & J.N.Hewitt, (Dordrecht: Kluwer), 215
7. Ansari, R., et al. 1996, A&A, in press
8. Aubourg, E., et al. 1995, A&A, 301, 1
9. Bahcall, J. N., Flynn, C., Gould, A., & Kirhakos, S. 1994, ApJ, 435, L51
10. Boutreux, T., & Gould, A. 1996, ApJ, 462, 705
11. Gould, A. 1994, ApJ, 421, L71
12. Gould, A. 1995a, ApJ, 441, L21
13. Gould, A. 1995b, ApJ, 441, 77
14. Gould, A. 1996, PASP, 108, 465
15. Gould, A., Bahcall, J. N., & Flynn C. 1996, ApJ, 465, 759
16. Gould, A. & Welch, D. 1996, ApJ, 464, 212
17. Griest, K. 1991, ApJ, 366, 412
18. Han, C. & Gould, A. 1995, ApJ, 447, 53
19. Loeb A. & Sasselov, D. 1995, ApJ, 449, L33
20. Maoz, D., & Gould, A. 1994, ApJ, 425, L67

21. Mihalas, D., & Binney, J., 1981, *Galactic Astronomy*, (New York: W. H. Freeman)
22. Nemiroff, R. J., & Wickramasinghe, W. A. D. T. 1994, *ApJ*, 424, L21
23. Paczyński, B. 1986, *ApJ*, 304, 1
24. Udalski, A. et al. 1994, *Acta Astron*, 44, 165
25. Witt, H. 1995, *ApJ*, 449, 42
26. Witt, H. & Mao, S. *ApJ*, 430, 505